Self-Calibration of a Network of Radar Sensors for Autonomous Robots

Timo Grebner, Graduate Student Member, IEEE
Institute of Microwave Engineering, Ulm University

Vinzenz Janoudi, Graduate Student Member, IEEE
Institute of Microwave Engineering, Ulm University

Pirmin Schoeder, Graduate Student Member, IEEE
Institute of Microwave Engineering, Ulm University

Christian Waldschmidt, Fellow, IEEE
Institute of Microwave Engineering, Ulm University

***Abstract*— Radar sensor networks are today widely used in the field of autonomous driving and for generating high-precision images of the environment. The accuracy of the environmental representation depends to a large extent on the accurate knowledge of the sensor's mounting orientation. Both the relative orientation of the sensors to each other and the relative sensor orientation in relation to the vehicle coordinate system are determining factors. For the first time, the orientation estimation of the radar sensors of a network is possible exclusively on the basis of radar target lists without additional localization and orientation devices such as an IMU or GNSS. In this work, two algorithms for determining the orientation of incoherently networked radar sensors with respect to the vehicle coordinate system and with respect to each other are derived and characterized. With the presented algorithms orientation accuracies up to 0.25° are achieved. Furthermore, the algorithms do not impose any requirements on the positioning or the orientation of the radar sensors, such as overlapping field of views (FOVs) or the detection of identical targets. The presented algorithms are applicable to arbitrary driving trajectories as well as for point targets and extended targets which enables the use in regular road traffic.**

***Index Terms*— chirp-sequence radar sensors, ego-motion estimation, orientation estimation, radar imaging sensors, radar sensor networks, self-calibration**

I. INTRODUCTION

MODERN high-level systems for autonomous driving are based on highly precise environmental recognition as well as accurate speed and position information, which can be estimated very robustly with lidar sensors, cameras or radar sensors, respectively [1], [2]. The focus of research in this area has changed only in recent years from the use of a single sensor system to the use of multiple sensors working cooperatively, especially in the field of radar sensors [3], [4]. In order to ensure high precision, both intrinsic error influences such as incorrect array calibration and extrinsic error influences such as incorrect orientation of the sensors, must be minimized. While there are various effective calibration methods for intrinsic error sources, [5], [6], [7], methods for extrinsic calibration are often costly or linked to certain prerequisites [8]. They exist in great diversity especially for both cameras [9], [10] and lidar sensors [11], [12].

In contrast, the approaches for radar sensors are usually based on many requirements. It has already been shown in [13] that the orientation of radar sensors mounted on a car can be determined with high precision based on ego-motion estimation. Furthermore, the orientation estimation can be extended for radar sensors with a 2D angle estimation [14]. However, this orientation estimation method requires an additional time-synchronized inertial measurement unit (IMU). A different approach to estimate the orientation of the radar sensors is based on the usage of high-precision environmental maps [15], wherein the current vehicle position and high-precision environmental maps must be available, which are generated by lidar and camera sensors [16], [17], [18] and global navigation satellite systems (GNSSs) [8]. In [19] it was shown that the accuracy of orientation estimation can be significantly improved using corner reflectors as radar targets. However, the position of the targets must be known. Approaches to estimate the orientation of the radar sensors on the car without using additional systems are based on the detection of identical targets and lead to rather inaccurate orientation estimates. For this purpose overlapping field of views (FoVs) of multiple radar sensors are required [20], [21] which limits the positioning flexibility of the individual radar sensors.

Using the algorithms presented in this paper, it is possible to estimate the orientation of N radar sensors ($N \geq 2$) relative to the vehicle coordinate system and in relation to the other radar sensors mounted on the same car. The algorithms are the first ones achieving this solely based on target lists and known relative sensor positions. The benefit of this approach is on the one hand, that no additional systems like GNSS or IMU are required for the estimation. On the other hand, the ego-motion based approach has no constraints regarding the positioning of the radar sensors, thus no overlapping FoV of the sensors and no multi-frame target detection are required.

The paper is organized as follows: the sensor setup and the basic steps of signal processing are presented in Sections II and III. The fundamentals of ego-motion estimation are presented in Section IV. Based on this, Section V describes two algorithms to determine the orientation of all sensors. The evaluation based on measurements as well as various robustness analyses are described in Section VII. The result of a Monte-Carlo simulation to analyze

The authors are with the Institute of Microwave Engineering, Ulm University, 89081 Ulm, Germany (e-mail: timo.grebner@uni-ulm.de).

Color versions of one or more of the figures in this article are available online at http://ieeexplore.ieee.org.

the sensor position dependent estimation accuracy of the sensor orientation is described in Section VIII.

II. Concept and System Architecture

The general concept consists of distributed chirp-sequence modulated MIMO radar sensors, which are used as an incoherent but time-synchronized network. The chirp-sequence radar sensors used transmit sequences of fast frequency-modulated continuous-wave (FMCW) ramps. Each chirp sequence consists of R FMCW ramps, which have a bandwidth of f_{B}, a ramp time of T_{c}, and a ramp repetition time of T_{r} [22], [23]. The time synchronization of all radar sensors of the network enables a simple interference avoidance as soon as the center frequency of all radar sensors is shifted by at least the IF bandwidth with respect to each other [24]. This time synchronization also enables a joint evaluation of all target lists for the orientation estimation.

The most relevant measurement quantities, which can be determined with such radar sensors are radial velocities $v^{\mathrm{r}}_{n,m}$, angles of arrival $\phi^{\mathrm{s}}_{n,m}$ and distances $r_{n,m}$ in the sensor coordinate system (^{s}) for the n-th sensor and the m-th target. These quantities can be determined with N radar sensors ($n \leq N$) for all M_n detected targets ($m \leq M$) of each individual sensor n.

The system setup comprises multiple radar sensors, which are installed around a vehicle with an unknown orientation $\varphi^{\mathrm{c}}_1, \ldots, \varphi^{\mathrm{c}}_N$ in the vehicle coordinate system (^{c}). A possible sensor configuration is shown in Fig. 1 for N=7 radar sensors and one target t_1. A wide spatial distribution of sensors provides a more accurate ego-motion estimation and a more flexible evaluation of the measurement results regarding the positioning and the number of sensors in Section VII and VIII.

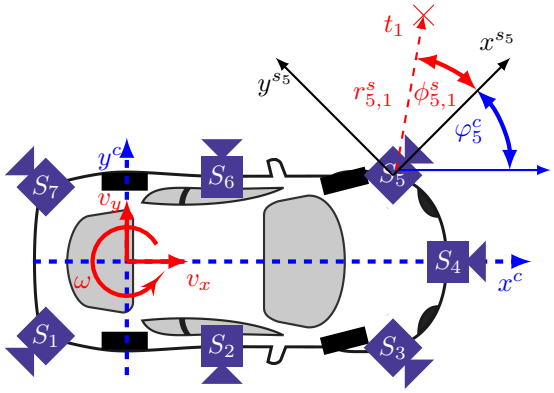

Fig. 1: Radar network with N=7 radar sensors in violet with orientations φ^c_n to be estimated. Vehicle coordinate system [x^c, y^c] in blue, dashed and corresponding velocity components in red, solid lines. Sensor coordinate system of S_5 in black [x^s, y^s] and an exemplary detected target t_1 with an AoA of $\phi^s_{5,1}$ and a range of $r^s_{5,1}$.

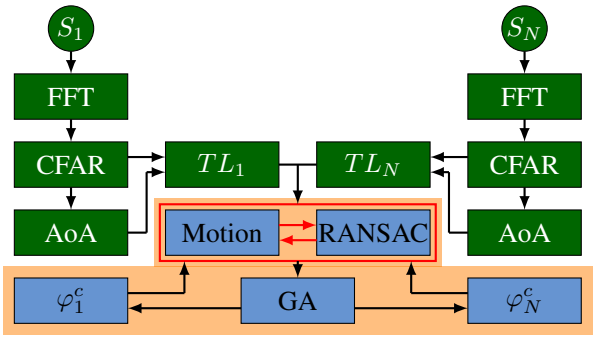

Fig. 2: Signal flow chart for extracting every sensor's target list (green) and estimating its orientation $\varphi^{\mathrm{c}}_1, \ldots, \varphi^{\mathrm{c}}_N$ (blue) for N radar sensors $(S_1, ..., S_N)$ based on ego-motion estimation (red).

III. Processing Chain

An overview of the signal processing chain is depicted in Fig. 2. The first steps are performed individually for each sensor and are illustrated as green boxes in Fig. 2. The raw data from N time-synchronized incoherently-connected radar sensors are stored, processed independently and transformed into the frequency domain using a fast Fourier transform (FFT). The relevant target information is extracted by using a constant false alarm rate (CFAR) algorithm, subsequent peak detection, and angle of arrival (AoA) estimation and is stored in individual target lists (TL). These basic signal processing steps for all N sensors are shown in Fig. 2 in green. In contrast, the blue elements describe the procedure of the orientation estimation algorithm and are described in more detail in the later part of this work.

Based on the individual target list of each sensor, stationary targets are filtered out and used for a precise estimation of the vehicle's proper motion, which is depicted in Fig. 1 as red box. The intrinsic velocity of a vehicle is generally described by the two velocity components v_{x} and v_{y} as well as the yaw rate ω, which is shown in Fig. 1. Based on ego-motion estimation and random sample consensus (RANSAC)-filtering, a genetic optimization algorithm (GA) is applied afterwards to estimate the orientation $\varphi^{\mathrm{c}}_1, \ldots, \varphi^{\mathrm{c}}_N$ of all N radar sensors which is depicted as orange box in Fig. 2. Therefore, first the basics of the ego-motion estimation are derived.

IV. Ego-Motion Estimation

The three velocity components v_{x} and v_{y} as well as the yaw rate ω are estimated using a radar sensor network with at least two radar sensors (N>2) based on target lists [25], [26], [27]. The following model describes the relationship between one sensor and the measured target

information $v^{\mathrm{r}}_{n,m}$, $\phi^{\mathrm{s}}_{n,m}$ and the ego-velocity.

$$\underbrace{\begin{bmatrix} -v^{\mathrm{r}}_{n,1} \\ -v^{\mathrm{r}}_{n,2} \\ \vdots \\ -v^{\mathrm{r}}_{n,M} \end{bmatrix}}_{\mathbf{V}^{\mathrm{r}}_{n}} = \underbrace{\begin{bmatrix} \cos\left(\phi^{\mathrm{c}}_{n,1}\right) & \sin\left(\phi^{\mathrm{c}}_{n,1}\right) \\ \cos\left(\phi^{\mathrm{c}}_{n,2}\right) & \sin\left(\phi^{\mathrm{c}}_{n,2}\right) \\ \vdots & \\ \cos\left(\phi^{\mathrm{c}}_{n,\mathrm{M}}\right) & \sin\left(\phi^{\mathrm{c}}_{n,\mathrm{M}}\right) \end{bmatrix}}_{\mathbf{A}_n} \cdot \underbrace{\begin{bmatrix} -y^{\mathrm{c}}_{n} & 1 & 0 \\ x^{\mathrm{c}}_{n} & 0 & 1 \end{bmatrix}}_{\mathbf{S}_n} \cdot \begin{bmatrix} \omega \\ v_x \\ v_y \end{bmatrix} \tag{1}$$

Here, $x^{\mathrm{c}}_{\mathrm{n}}$ and $y^{\mathrm{c}}_{\mathrm{n}}$ denote the sensor positions and $\phi^{\mathrm{c}}_{n,m}$ the AoA relative to the vehicle coordinate system. These relative AoAs are calculated with

$$\phi^{\mathrm{c}}_{n,m} = \phi^{\mathrm{s}}_{n,m} + \varphi^{c}_{n} \tag{2}$$

in order to transform the angles from the sensor coordinate system $\phi^{\mathrm{s}}_{n,m}$ to the vehicle coordinate system, in which case φ^{c}_{n} is the z orientation of the sensors on the vehicle, as shown in Fig. 1.

If more than one radar sensor (N>1) is used, the equations can be converted into a system of linear equations, and thus, the velocity vector of the vehicle's motion $\mathbf{V_p}$ can also be unambiguously determined with the help of:

$$\underbrace{\begin{bmatrix} \mathbf{V^r_1} \\ \mathbf{V^r_2} \\ \vdots \\ \mathbf{V}^{r}_{N} \end{bmatrix}}_{\mathbf{V^r}} = \underbrace{\begin{bmatrix} \mathbf{A_1} \cdot \mathbf{S_1} \\ \mathbf{A_2} \cdot \mathbf{S_2} \\ \vdots \\ \mathbf{A}_N \cdot \mathbf{S}_N \end{bmatrix}}_{\mathbf{M}} \cdot \underbrace{\begin{bmatrix} \omega \\ v_x \\ v_y \end{bmatrix}}_{\mathbf{V_p}} . \tag{3}$$

Equation (3) can be solved in the least square sense for the desired velocity vector $\mathbf{V_p}$ with the Moore-Penrose inverse ($^+$).

$$\mathbf{V_p} = \mathbf{M}^{+} \cdot \mathbf{V^r} \tag{4}$$

The vehicle speed is determined based on stationary targets using the dependency described in (3). For estimating the vehicle's speed, at least two sensors must detect a total of at least three targets to allow velocity estimation for all three degrees of freedom (DoFs). Since (3) is only valid for stationary targets, non-stationary targets as well as false detections have to be filtered out. These outliers, which do not satisfy the searched motion model, are filtered out in the following using a random sample consensus (RANSAC) algorithm [28].

A. RANSAC-Filtering

To provide a reliable and robust ego-motion estimation outliers must be filtered out for example with an iterative RANSAC-algorithm with I iteration steps. For this purpose, in each iteration step $i \leq I$ of the RANSAC algorithm, the velocity model $\mathbf{V}^{i}_{\mathbf{p}}$ is estimated based on three randomly chosen targets from the target lists $(\mathrm{TL}_1, ..., \mathrm{TL}_N)$ and subsequently the difference $\mathbf{D}$ to all measured radial velocities $\mathbf{V_r}$ is determined.

$$\mathbf{D}^{i} = \left| \mathbf{M} \cdot \mathbf{V}^{i}_{\mathbf{p}} - \mathbf{V_r} \right| \tag{5}$$

Subsequently, the quality of the velocity estimate is assessed on the basis of the number of inliers K in (6). Inliers indicate targets that have a smaller velocity error than a suitable threshold T regarding the currently estimated motion model. The threshold has to be chosen in a way that a majority of all real stationary targets are within the threshold despite measurement inaccuracies and noise. To ensure this, a threshold of T=0.1 $\frac{\mathrm{m}}{\mathrm{s}}$ is chosen for the evaluation. This iterative RANSAC process is described by

$$K = \arg\max_{i \leq I} \left(\sum_{j=1}^{J} \mathbb{1}_{(D^{i}_{j} < T)} \right) \tag{6}$$

where D_j describes the j-th element ($j \leq J$, J=$O(\mathbf{D})$ where O describes the cardinality) of the vector $\mathbf{D}$ with

$$\mathbf{D} = \begin{bmatrix} D_1 & D_2 & \dots & D_{\mathrm{J}} \end{bmatrix}^{\mathrm{T}} \tag{7}$$

and $\mathbb{1}$ specifies the indicator function with:

$$\mathbb{1}_{(D_j < T)} = \begin{cases} 1 & D_j \leq T \\ 0 & \text{otherwise.} \end{cases} \tag{8}$$

The model which fits best to the current measurement, and thus has the most inliers, corresponds to the most probable velocity vector $\mathbf{V}^{K}_{\mathbf{p}}$ of all I iteration steps.

Since the RANSAC filtering is based on I iteration steps and three randomly chosen targets, $\mathbf{V}^{K}_{\mathbf{p}}$ only describes the best estimate based on three stationary targets but not based on all stationary targets. To improve the velocity estimation, the vehicle velocity is estimated again based on all targets that satisfy the model within the threshold tolerance T for the velocity vector $\mathbf{V}^{K}_{\mathbf{p}}$.

V. Orientation Estimation

According to the equation of the velocity model (1) and the subsequent conversion to the vehicle coordinate system (2), it is evident that the velocity estimate is significantly dependent on the orientation of the sensors. Thus, the quality of the velocity estimation described in (1) is used to determine the most likely velocity for a given combination of sensor orientations $\varphi^{\mathrm{s}}_1, \dots, \varphi^{\mathrm{s}}_N$. Therefore, the algorithm can be extended to estimate not only the velocity vectors, but also the orientation of all radar sensors installed on the vehicle. The approach is shown as a schematic in Fig. 2 in the orange-filled area and is explained in more detail in the following.

A. Basic Orientation Estimation (BOE)

For the purpose of orientation estimation, a function is initially set up that reflects the quality of the velocity estimation for different sensor orientations $\varphi^{\mathrm{c}}_1, \dots, \varphi^{\mathrm{c}}_N$. This can be achieved by extending (5) for arbitrary sensor orientations $\varphi^{\mathrm{c}}_1, \dots, \varphi^{\mathrm{c}}_N$, which determines the difference of all targets to a given velocity vector $\mathbf{V}^{K}_{\mathbf{p}}$ and given sensor orientation $\varphi^{\mathrm{c}}_1, \dots, \varphi^{\mathrm{c}}_N$.

$$\mathbf{D}^{i,\varphi} = \mathbf{D}^{i}\left(\varphi^{\mathrm{c}}_{\mathbf{1}}, \dots, \varphi^{\mathrm{c}}_{\mathbf{N}}\right) = \left| \mathbf{M}\left(\varphi^{\mathrm{c}}_{\mathbf{1}}, \dots, \varphi^{\mathrm{c}}_{\mathbf{N}}\right) \cdot \mathbf{V}^{i}_{\mathbf{p}} - \mathbf{V_r} \right| \tag{9}$$

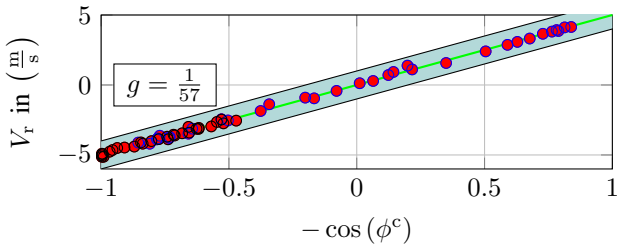

(a) $\varphi_\mathrm{est} = [0°\ 90°]$.

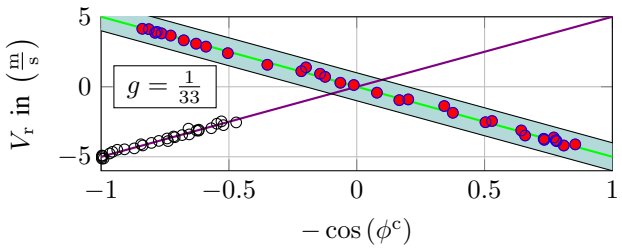

(b) $\varphi_\mathrm{est} = [0°\ \ -90°]$.

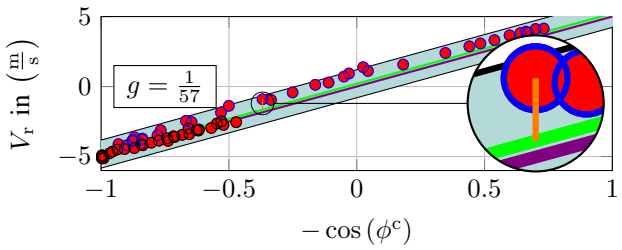

(c) $\varphi_\mathrm{est} = [0°\ 80°]$.

Fig. 3: Representation of the ground truth motion and the ego-motion estimation based on detected targets of a simulated straight line drive for sensors with the ground truth sensor orientations $\boldsymbol{\varphi}_\mathbf{GT} = [\varphi_1\ \varphi_2] = [0°\ 90°]$ and the corresponding inliers.

Based on equation (9), identical to the ego-motion estimation, the most probable vehicle speed $\mathbf{V}_\mathbf{p}^K$ for a specific orientation of the radar sensors $\boldsymbol{\varphi}$ is estimated by using the RANSAC algorithm described in (6) another time.

$$K = \underset{i \leq I}{\arg\max} \left(\sum_{j=1}^{J} \mathbb{1}_{\left(D_j^{i,\boldsymbol{\varphi}} < T\right)} \right) \tag{10}$$

However, since the most likely sensor orientation $\varphi_1^\mathrm{c}, \ldots, \varphi_N^\mathrm{c}$ is now of interest rather than the most likely vehicle velocity, equation (10) must be extended by a further minimization over all possible orientation angles $\varphi_1^\mathrm{c}, \ldots, \varphi_N^\mathrm{c}$. The most probable sensor orientation is given once the number of inliers is maximal, which is described by the following equation:

$$\boldsymbol{\varphi}_\mathbf{est} = \underset{\left(\varphi_1^\mathrm{c}, \ldots, \varphi_N^\mathrm{c}\right)}{\arg\min}\ (g) \tag{11}$$

$$g = \frac{1}{\sum\limits_{F} \max\limits_{i \leq I} \left(\sum_{j=1}^{J} \mathbb{1}_{\left(D_j^{i,\boldsymbol{\varphi}} < T\right)} \right)} \tag{12}$$

This principle is illustrated by Fig. 3a and 3b based on a radar sensor network with $N{=}2$ sensors. The two sensors have a ground truth orientation of $\boldsymbol{\varphi}_\mathbf{GT} = [\varphi_1\ \varphi_2] = [0°\ 90°]$ and detect arbitrary targets. The x-axis represents the angle of arrival in relation to the vehicle coordinate system, and the y-axis represents the measured radial velocity. Each point represents a target, detected by sensor S_1 (black) or sensor S_2 (blue).

A RANSAC-based ego-motion estimation with the ground truth sensor orientations as shown in Fig. 3a provides a robust velocity estimate based on many inliers (red filled), which lie within an appropriate threshold (turquoise). These inlier represent stationary targets (black for sensor 1, blue for sensor 2) that correspond to the velocity model. Once the estimation is performed based on identical targets but with incorrect sensor orientations, as shown in Fig. 3b, an ego-motion estimation, depicted as green line in Fig. 3b, can still be performed in this scenario, but it differs from the correct velocity estimation which is depicted as violet line in Fig. 3b. The blue targets are the same one as the ones depicted in Fig 3a but with a different calculated AoA in relation to the vehicle coordinate system due to the orientation of the sensor.

In addition, the estimate does not have the same quality because the number of inliers has been significantly reduced since the inliers only include targets of the second sensor which is depicted in blue. As a result of the reduced number of inliers, the value for the error function of g in (12) increases from $g{=}1/57$ to $g{=}1/33$, resulting in a less accurate and more implausible ego-motion, and thus a more improbable orientation estimate.

Since the orientation does not change during a measurement run over several frames F, multiple frames can be used for improved robustness. Therefore, the optimal velocity is estimated for each frame based on the sensor orientations $\varphi_1^\mathrm{c}, \ldots, \varphi_N^\mathrm{c}$ and the resulting number of inliers is determined. Numerical minimization of the function g with a GA yields the orientation of the sensors.

To solve the general mathematical problem unambiguously, the vehicle velocity estimation must be restricted to a maximum of two degrees of freedom ω and v_x, whereby v_y is not estimated and is assumed to be 0. Therefore (1) is simplified to:

$$\underbrace{\begin{bmatrix} -v_{n,1}^\mathrm{r} \\ -v_{n,2}^\mathrm{r} \\ \vdots \\ -v_{n,M}^\mathrm{r} \end{bmatrix}}_{\mathbf{V}_n^\mathrm{r}} = \underbrace{\begin{bmatrix} \cos\left(\phi_{n,1}^\mathrm{c}\right) & \sin\left(\phi_{n,1}^\mathrm{c}\right) \\ \cos\left(\phi_{n,2}^\mathrm{c}\right) & \sin\left(\phi_{n,2}^\mathrm{c}\right) \\ \vdots & \\ \cos\left(\phi_{n,\mathrm{M}}^\mathrm{c}\right) & \sin\left(\phi_{n,\mathrm{M}}^\mathrm{c}\right) \end{bmatrix}}_{\mathbf{A}_n} \cdot \underbrace{\begin{bmatrix} -y_n^\mathrm{c} & 1 \\ x_n^\mathrm{c} & 0 \end{bmatrix}}_{\mathbf{S}_n} \cdot \begin{bmatrix} \omega \\ v_x \end{bmatrix}. \tag{13}$$

This equation of motion can still be used to describe both a straight-line and a curved trajectory. Once the trajectory has no curves and is only linear, the equation of motion (13) can be further simplified to estimate only the v_x

component, reducing the DoFs even further.

$$\underbrace{\begin{bmatrix} -v^{\mathrm{r}}_{n,1} \\ -v^{\mathrm{r}}_{n,2} \\ \vdots \\ -v^{\mathrm{r}}_{n,M} \end{bmatrix}}_{\mathbf{V}^{\mathrm{r}}_{n}} = \underbrace{\begin{bmatrix} \cos\left(\phi^{\mathrm{c}}_{n,1}\right) \\ \cos\left(\phi^{\mathrm{c}}_{n,2}\right) \\ \vdots \\ \cos\left(\phi^{\mathrm{c}}_{n,\mathrm{M}}\right) \end{bmatrix}}_{\mathbf{A}_{n}} \cdot \begin{bmatrix} v_x \end{bmatrix} \tag{14}$$

Since a straight-line trajectory with ω=0 is difficult to realize in reality, this simplification is used exclusively for evaluation and comparison of straight-line trajectory and curved trajectory in Section VII.

The restriction to a maximum of two DoFs results from the fact that as soon as there is only a linear motion of the car (only v_{x} and v_{y}) an identical sensor orientation offset of h degree for all N sensors still leads to a linear motion of the car, but the cars movement vector is rotated by h degree. This results in different velocity estimates for different sensor orientations. The problem in this case is that this incorrect speed cannot be distinguished from the correct speed, since the number of inliers is identical in both cases.

This problem can be clearly seen in Fig. 1. For a vehicle having only v_x velocity, a local v^s_x velocity in sensor coordinates is estimated for the sensor S_4 according to equation 1. Once the vehicle velocity is not restricted to v_x and ω only, and the orientation of the sensors has to be estimated, the sensor S_4 could also have the orientation of S_6, and thus be rotated by 90°. In this case, a local v^s_x velocity of the sensor is still estimated in sensor coordinates, but this results in a v_y velocity in vehicle coordinates. This ambiguity can thus only be resolved by restricting the vehicle motion in v_x and ω. Since vehicles drift only minimally even while cornering [29] and thus $v_{\mathrm{y}}{\approx}0$ holds, in the following the velocity vector to be estimated is restricted to v_x and ω analogue to (13) to eliminate the ambiguities of the orientation estimation.

As the orientation estimation is based on the quality of the ego-motion estimation the solution of the orientation estimation is unambiguous as soon as the local velocity of each sensor (v^s_x and v^s_y) can be determined unambiguously. This is guaranteed as soon as each of the N sensors detects at least M=2 targets [25], [26], [27].

B. Advanced Orientation Estimation (AOE)

This type of orientation estimation (BOE) described in (12) is limited with respect to its maximum achievable accuracy, as can be seen in Fig. 3c. If the sensor S_2 has only a small orientation deviation from the ground-truth orientation (for improved illustration $\Delta\varphi_2$=10°), all targets are still detected as inliers (for the chosen threshold). Because of that, the function g has an identical quality factor with g=1/57 for both correct (Fig. 3a) and incorrect orientations (Fig. 3c). The minimization of the function g and thus the estimated sensor orientation is randomly distributed around the ground truth orientation within a small tolerance, the chosen threshold for ego-motion estimation, which is shown in the later measurement section VII.

In order to provide a more robust and consistent estimate of orientation, an even finer orientation search based on a least-square optimization of the velocity errors can be performed after applying the basic orientation algorithm described in Section V. Since the maximum number of inliers, which corresponds to the minimum of the function g, is known from the previous estimation calculated with (12), the errors between the estimated radial velocity and the measured radial velocity are minimized for all inliers. The boundary conditions are the number of inliers known from (12), which is described by the following equation

$$\boldsymbol{\varphi}_{\mathbf{est}} = \underset{\left(\varphi^{\mathrm{c}}_1,\ldots,\varphi^{\mathrm{c}}_N\right)}{\arg\min} \left(\sum_{F} \sum_{j=1}^{J} \mathbb{1}_{\left(D^{i,\boldsymbol{\varphi}}_j < T\right)} \cdot D^2_j \right) \Bigg|_{\substack{\min \\ \left(\varphi^{\mathrm{c}}_1,\ldots,\varphi^{\mathrm{c}}_N\right)}}^{(g)} . \tag{15}$$

This deviation is exemplarily shown in orange in Fig. 3c for one target. This LSQ-based optimization yields the more precise motion estimation and therefore the more precise and reliable orientation estimation. Moreover, relative to numerical minimization deviations, a more robust and unambiguous orientation estimation can be provided, which reliably yields similar results and is shown in Section A.

VI. Measurement Setup

The measurement setup to verify the theoretical derivations is shown in Fig. 4 and consists of seven incoherently connected chirp-sequence radar sensors [24]. The measurement setup corresponds to the sketch in Fig. 1. The sensors are mounted approximately equiangularly around the vehicle in 45° steps, providing a 360° field of view (FoV). The ground truth of the sensor positions relative to the vehicle coordinate system were determined using a Trimble tachymeter.

Fig. 4: Experimental system setup with seven chirp-sequence radar sensors mounted on a car.

The measurement run was performed on a parking lot with not only stationary targets but also non-stationary targets such as moving cars or pedestrians, which are filtered out using the RANSAC algorithm described in Section IV. No additional targets such as corner reflectors were set up in the parking lot. Thus, the following evaluations

TABLE I: Used Radar Parameters for Ego-Motion-Based Self-Calibration.

Parameter	**Value**			
	S_1	S_2	S_3	S_4
Start frequency (GHz)	77.22	77.25	77.28	77.34
Approx. Orientation φ_n^c (°)	−135	−90	−45	0
	S_5	S_6	S_7	
Start frequency (GHz)	77.37	77.40	77.43	
Approx. Orientation φ_n^c (°)	45	90	135	
Bandwidth	3.07 GHz			
Ramp repetition time	67 µs			
Sampling frequency (IQ)	10 MHz			
Number of ramps (per Tx)	128			
Max. unambiguous velocity	4.823 $\frac{\mathrm{m}}{\mathrm{s}}$			
Number of transmitters	3			
Number of receivers	4			
Measurement rate	37 Hz			

are based exclusively on extended targets (vehicles, trees, wooden fences, branches, gravel, and lampposts). For the time synchronization of the radar sensors an external trigger is used. In combination with a small variation of the sensors' start frequencies, the time synchronization can be used for interference suppression between the sensors [30]. Due to identical radar parameters, apart from the start frequency of each sensor, the transmit ramps of all sensors have a constant frequency offset between each other. Thus, no intersection between the ramps and therefore no interference in the IF band is to be expected. The radar parameters are listed in Table I.

The ground truth orientations of the sensors have been determined using an IMU-based algorithm. It was shown that with the help of an IMU the orientation of radar sensors can be estimated with an accuracy of about $0.05°$ [13]. Thus, the accuracies of the algorithm described in this work are compared to the orientation estimates from [13]. These are assumed as ground truth values in the following.

VII. Measurement Results

At first, the basic orientation estimation algorithm described in (12) and the advanced orientation estimation algorithm described in (15) are compared to each other. Afterwards, the robustness with respect to the number of sensors, the number of frames, the sensor orientation and sensor positioning are investigated and verified based on measurements and simulations.

A. Comparison of Orientation Estimation Algorithms: BOE vs AOE

In Section V two different methods for the orientation estimation based on target lists were presented: first, the BOE algorithm which maximizes the number of inliers as described in (12), and second the AOE algorithm, an approach to minimize the squared error between the found inliers and the estimated velocity (15).

The results of a measurement run with a straight-line trajectory, N=7 sensors and F=1000 frames are shown in Fig. 5.

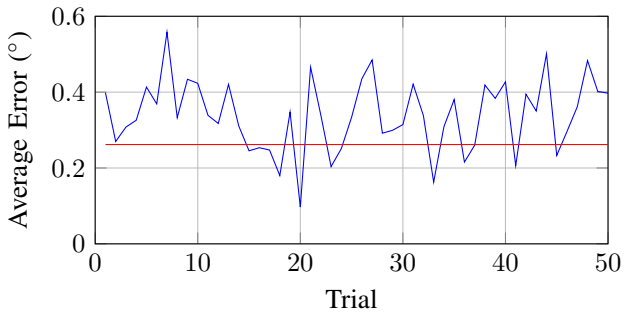

Fig. 5: Average orientation estimation accuracy for N=7 sensors and F=1000 frames based on the BOE algorithm (blue) and the AOE algorithm (red).

In order to show the advantages of the least square based AOE-method (red curve) compared to inlier number based BOE-method (blue curve) described in Section V, 50 trials of the identical measurement run were performed. In Fig. 5 it can clearly be seen that as soon as only the number of inliers is used for the orientation estimation, the results of the orientation estimation vary, although the same number of inliers was always found using the GA. This has already been visualized in Fig. 3c. The variance depends on the chosen threshold T, which in turn has to be adapted to the quality of the measurements and thus to standard deviations σ_{v^r} and σ_ϕ. Using the BOE algorithm, the orientation of the sensors can be determined with an accuracy of $0.34°$ on average, with a standard deviation of about $0.1°$. In contrast to this, the least square based AOE method (red curve) provides a reliable and constant (within the numerical minimization limits) solution, which is better with only $0.26°$ deviation and thus about $33\,\%$ more accurate.

In relation to an orientation estimation based on high-precision maps , which achieves an orientation accuracy of about $0.5°$ for each sensor [15], the error can be reduced by a half with the algorithm presented in this work. A comparison with the angle estimation accuracy of the radar sensors illustrates the quality of the orientation estimation algorithm.

The standard deviation of the angle estimation of the used radar sensors, which have an aperture size in azimuth direction of 4λ corresponds to $\sigma_\Phi \approx 1.2°$ for a target with an SNR of $40\,\mathrm{dB}$ and can be calculated with [31]

$$\sigma_\Phi = \frac{\Delta\Phi_{3\mathrm{dB}}}{1.6\sqrt{2\,(\mathrm{SNR})}}. \tag{16}$$

The presented orientation estimation algorithm enables an orientation estimate exclusively based on target lists which is significantly more accurate than the angular accuracy of the radar sensor.

B. Comparison of Different Trajectories

According to Section V, the described algorithms are only limited by the condition that the lateral vehicle velocity must be zero (v_y=0). Since this can be assumed corresponding to [29] also for curved trajectories, the algorithm is applicable for both straight-line and curved trajectories.

The average orientation errors for a different number of sensors and different trajectories is shown in the following Fig. 6. In each case, 50 different trials with a length of F=1000 frames were evaluated.

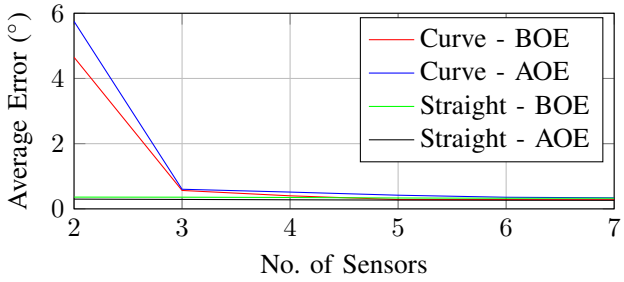

Fig. 6: Average orientation estimation error for different number of sensors, and trajectories.

For the straight-line trajectory, only the x-component of the velocity vector $\mathbf{v_p}$ was estimated according to (14), whereas for the curved trajectory, the velocity components v_x and ω are estimated according to (13).

Analogously to Fig. 5, it is noticeable how the least square based AOE solution method provides accuracy advantages in all categories compared to the inlier number-based BOE solution method. Moreover, it can be seen in Fig. 6 that for a straight trajectory, as the number of N sensors increases, the estimation error improves only marginally from 0.30° with N=2 to 0.26° with N=7. For curved trajectories, the estimate improves significantly from 4.65° with N=2 to 0.28° with N=7 sensors.

In particular, the relatively poor estimation for N=2 sensors with curved trajectories is remarkable, which is shown and investigated in more detail in the following Fig. 7. This represents the logarithmic error of the function g for straight-line and curved trajectories and different number of sensors.

All figures in Fig. 7 are based on identical measured raw data from a straight-line trajectory with F=1000 frames. Fig. 7a and 7b plot the error function g logarithmically for, N=2 and N=7 sensors, respectively, with only sensors S_1 (x-axis) and S_2 (y-axis) shown. The minimum of the function in both cases can be clearly seen at approximately φ_1=234.5° and φ_2=271.5°. However, it is noticeable that once multiple sensors are used as in Fig. 7b, a much sharper and clearer minimum exists, thus resulting in a more precise and robust orientation estimate.

Once the identical straight-line trajectory is evaluated with the two DoF v_x and ω, and thus for arbitrary trajectories, significant differences can be detected. The results for N=2 sensors is depicted in Fig. 7c whereby

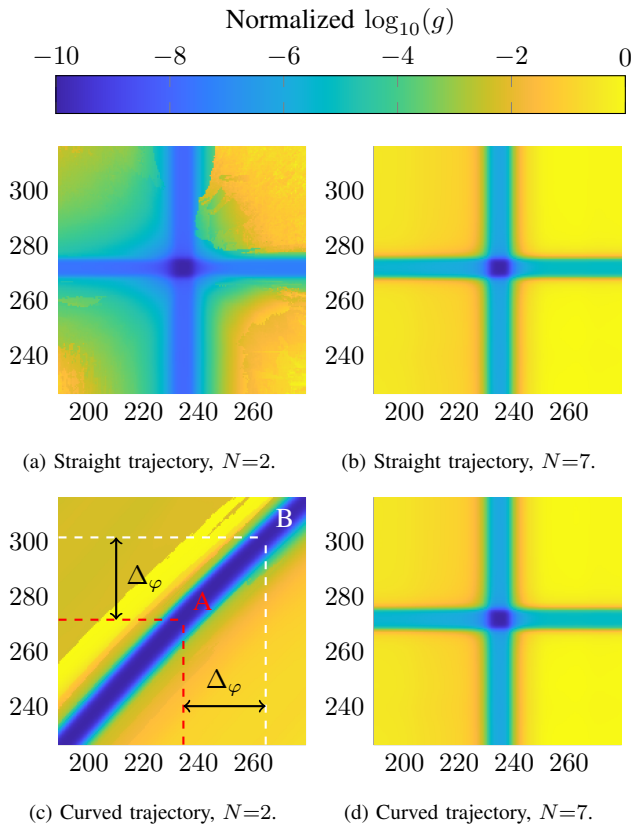

(a) Straight trajectory, N=2. (b) Straight trajectory, N=7.

(c) Curved trajectory, N=2. (d) Curved trajectory, N=7.

Fig. 7: Logarithmic representation of the error function g for straight-line trajectories (top) and curved trajectories (bottom) and N=2 sensors (left) and N=7 sensors (right). x-axis corresponds to the orientation φ_1 of sensor S_1 and y-axis corresponds to the orientation φ_2 of sensor S_2 in degrees for the measurement setup from Fig. 4.

the result for N=7 sensors is shown in Fig. 7d. As soon as only two sensors are used for the self-calibration, there is no definite global minimum of the function g but several minima, which all have similar values of the function g. All sensor orientations with similar minima of the function g have the property that the relative angle between the sensors, is still estimated correctly and thus the angular offset $\Delta\varphi$ is almost identical for both sensors. This is shown accordingly in Fig. 7c by mark A for the ground truth orientation, and mark B for a possible estimated orientation.

Thus, even with two sensors, the relative orientation of the sensors to each other can be estimated very well for curved trajectories, but precise orientation estimation relative to the vehicle coordinate system is highly error-prone. Since these figures represent the error function of a straight-line trajectory for the solution based on an arbitrary trajectory with the two DoFs, v_x and ω according to (13), the problem is of mathematical nature and not trajectory related. However, as soon as more than N=2 sensors are used, as shown in Fig. 7d for N=7 sensors, a definite minimum and thus a definite orientation of the

sensors in relation to the vehicle coordinate system can be determined for curved trajectories as well.
It should be noted that this phenomenon is not due to curved trajectories, but due to ambiguities in the ego-motion based orientation estimation with two degrees of freedom. Therefore, as seen in Fig. 7c, the phenomenon can also be detected for straight-line trajectories with 2DoF velocity estimation.
Since the algorithm is based on ego-motion estimation and not based on the detection of identical targets, it is not necessary to evaluate multiple frames, which also allows online calibration.

C. Online Calibration

Since the orientation of all sensors on the vehicle does not change during a measurement of several frames, the orientation can also be performed on the basis of several frames, which leads to an integration gain. The average error $\overline{\Delta\varphi}$ for the joint estimation of N=7 sensors is shown in Fig. 8 for 100 different sub sequences. Since it was shown in Section A that the accuracy can be improved using the AOE compared to the BOE algorithm, only the AOE method is shown.

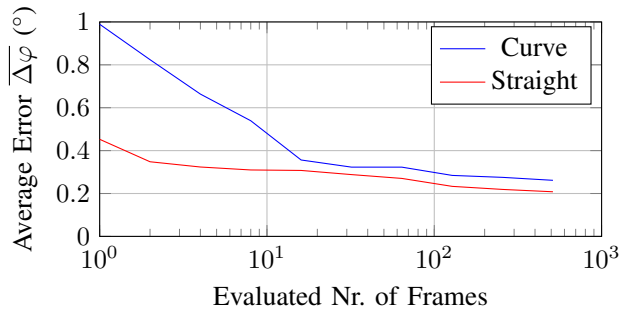

Fig. 8: Average orientation estimation error for different numbers of evaluated frames and trajectories.

The integration gain from evaluating multiple frames can be seen for both the straight trajectory with 1 DoF motion estimation and the curved trajectory with 2 DoF motion estimation. According to the previous findings from Section A and B, the evaluation of multiple frames provides significantly more advantages for the curved trajectory than for the straight trajectory due to the more ambiguous solution of the problem. However, depending on the required precision, the sensor orientation φ_n^c can be estimated independently of the trajectory even with only one frame to at least 1°.
Furthermore, it becomes apparent that the orientation estimation has a bias error of approximately 0.26° regardless of the number of sensors (Fig. 6) and regardless of the frames evaluated (Fig. 8). There are three main factors causing this offset:

- Incorrect measured sensor position
- Incorrect internal radar calibration
- Elevated targets

TABLE II: Used Simulation Parameters.

Figure	No. of Sensors	Sensor Position of Fixed Sensors (m)	Trajectory
9a	2	(3|0)	curve
9b	2	(0|1)	curve
9c	2	(3|0)	straight
9d	3	(3|0), (0|1)	curve

Incorrectly measured sensor positions lead to incorrect conversion from the sensor coordinate system to the vehicle coordinate system, especially in the case of curved trajectories. Furthermore, incorrect internal calibration leads to a nonlinear error in the AoA estimation. Ultimately, the algorithm is based on the assumption of non-elevated targets (θ=0°). With 1D angle estimation as used for the radar sensors employed, incorrectly estimated angles of arrival are the consequence for elevated targets. Once these errors do not occur a bias-free orientation estimation is possible as shown in Fig. 9 for simulation results.

VIII. Quality Criteria for Optimal Sensor Placement

The accuracy of the orientation estimation does not only depend on the trajectory, the number of sensors and the algorithm used, but also on the sensor constellation. In order to investigate the influence of the sensor constellation, a total of four different sensor configurations with two or three sensors as well as straight and curved trajectories, were evaluated according to Table II. Due to the large number of position and orientation possibilities, the valuation is based on simulation data.
The error of the orientation estimation by applying the AOE algorithm for multiple sensor configurations is illustrated in Fig. 9 for F=200 evaluated frames and 250 Monte Carlo trials with randomly generated target lists. All subfigures 9a, 9b, 9c and 9d indicate possible sensor positions and sensor orientations and the corresponding logarithmic average orientation estimation error in degree of all N sensors of the network. The x- and y-axes correspond to the vehicle coordinate system according to Fig. 1 and thus denote the x_n and y_n position of the respective sensor with respect to the origin of the vehicle coordinate system, at the center of the rear axle. All subfigures in Fig. 9 represent consequently a car with dimensions $5.5\,\mathrm{m} \times 2.5\,\mathrm{m}$, which is clarified exemplarily with a smaller car in Fig. 9c.
In order to reduce the complexity of the simulation, the orientation of the sensors is calculated according to the relative distance between sensor and vehicle rotation point:

$$\varphi_\mathrm{n} = \mathrm{atan2}\left(x_\mathrm{n}, y_\mathrm{n}\right). \tag{17}$$

The function atan2 is the four-quadrant 2-argument ambiguity-free arctangent. This corresponds to an omni-directional view of the sensors and is shown in Fig. 9c as an example for a sensor $S_{2,\mathrm{v}}$ in white. Thus, each x_n^c and y_n^c pixel corresponds to a sensor position and to a sensor orientation corresponding to a specific sensor orientation.

This article has been accepted for publication in IEEE Transactions on Aerospace and Electronic Systems. This is the author's version which has not been fully edited and content may change prior to final publication. Citation information: DOI 10.1109/TAES.2023.3277427

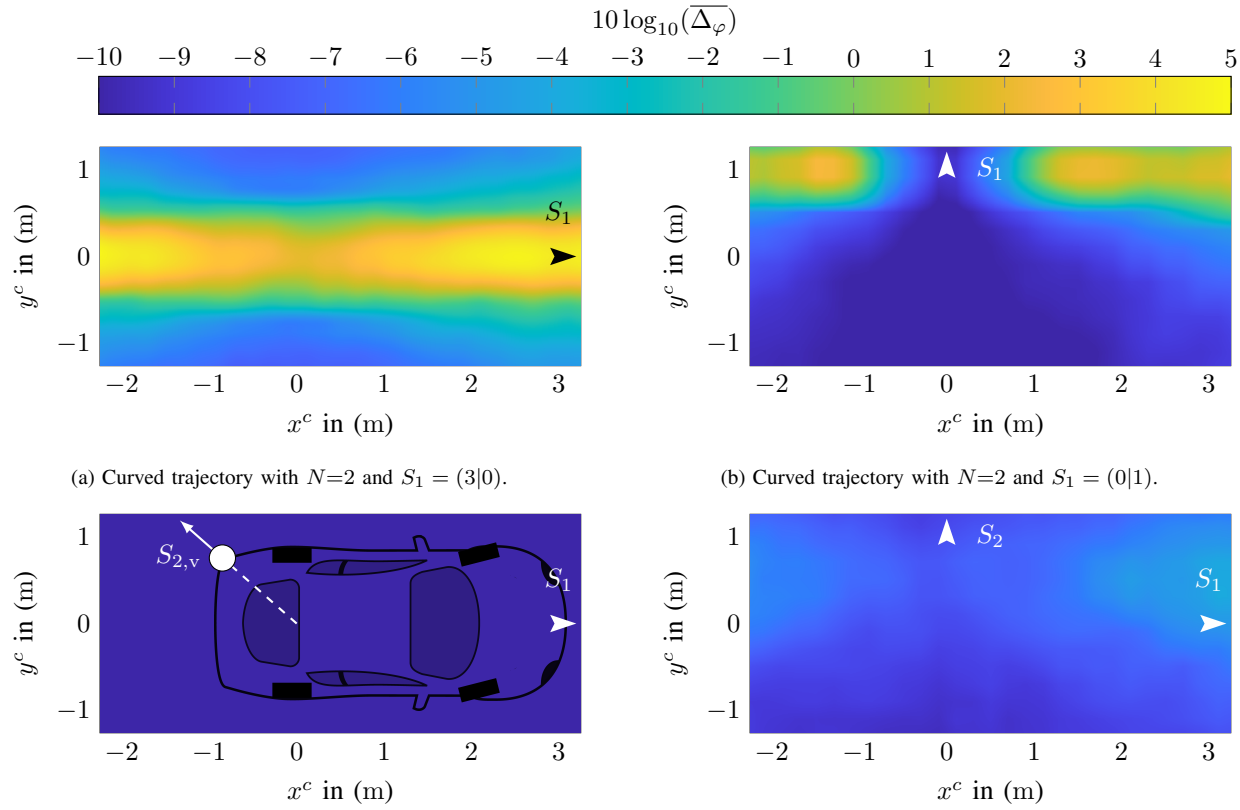

(a) Curved trajectory with N=2 and $S_1 = (3|0)$.

(b) Curved trajectory with N=2 and $S_1 = (0|1)$.

(c) Straight trajectory with N=2 and $S_1 = (3|0)$.

(d) Curved trajectory with N=3 and $S_1 = (3|0)$, $S_2 = (0|1)$.

Fig. 9: Average logarithmic orientation error for different trajectories, sensor poses S_1, S_2, S_3, and number of sensors. The position and orientation of all $N-1$ fixed sensors are indicated by arrows. The N-th sensor is variable and is located at the x_n^c and y_n^c position of the vehicle in the vehicle coordinate system and represents the logarithmic average orientation estimation error.

Since the structure of all subfigures is identical, the structure is described exemplarily according to Figure 9c. Figure 9c describes the orientation estimation accuracy for a radar sensor network with N=2 sensors, whereby the N-th sensor is variable with respect to position and orientation, and all other $N-1$ sensors are fixed positioned and orientated. The fixed sensors are always shown as triangles. In Fig. 9c, this is sensor S_1 at the front of the hood. The N-th sensor S_N (in Fig. 9c exemplary $S_{2,\mathrm{v}}$) is located at arbitrary x_n^c and y_n^c positions. The z-value at which the N-th sensor is located describes the averaged logarithmic orientation estimation error of all N radar sensors in this network. In that case, the average error for the fixed sensor S_1, which is always located at the front of the vehicle in Figure 9c, and the variable sensor S_2, which is located for example at the rear left bumper is $-1\widehat{=}0.1°$.

Fig. 9a illustrates the average orientation error for a sensor network consisting of N=2 sensors for a curved trajectory, where one sensor is located at position $[x_1^c, y_1^c]$=$[3\,\mathrm{m}, 0\,\mathrm{m}]$ with orientation φ_1=0°. The second sensor is arbitrarily positioned and oriented at position x_n^c and y_n^c according to Fig. 9a. The average orientation estimation error for both sensors and all 250 Monte Carlo trials per combination is plotted logarithmically at the position of the second sensor. The colorbar of the z-axis reflects errors between 0.1° and 3.1°.

Fig. 9a shows that as soon as sensor S_2 has a similar y component as sensor S_1 with $y_n^c \approx 0$, the orientation error is highest. According to (1), the motion model of each sensor has only a v_x^c and v_y^c component, which in combination with N sensors can be transferred into the motion model of the car with $\mathbf{V_P}$=$[\omega, v_\mathrm{x}, v_\mathrm{y}]$.

This transfer only works if at least N=2 radar sensors are used, otherwise the system of equations is underdetermined. According to (1), the robustness of the partitioning of sensor speeds into vehicle speeds is proportional to the distance between sensors. Since v_y=0 holds for the vehicle velocity in y-direction, only the difference of the y_n-component is significant. Similar y components lead to a broad minimum of the function g according to Fig. 7c, which leads to less accurate absolute orientation estimates.

As soon as the sensor S_2 is positioned near the rotation point $[0, 0]$ of the vehicle, the orientation of both sensors can be estimated much better, since the yaw rate with

respect to the sensor S_2 is decoupled according to (1). Furthermore, it can be seen that the estimation yields the best result as soon as both sensors are oriented in different directions with an orientation difference of $\varphi_2 = \pm 90°$. The identical phenomenon can also be seen in Fig. 9b for a curved trajectory in which the sensor S_1 is located on the left side of the vehicle $[x_1, y_1]=[0\,\mathrm{m}, 1\,\mathrm{m}]$ and exhibits an orientation of $\varphi_1 = +90°$. As soon as the two sensor orientations to be estimated have similar y-positions, the accuracy of the orientation estimation decreases.

The orientation estimation of the sensors can be significantly improved as soon as the vehicle has only a v_x velocity and thus only a straight trajectory exists. As soon as this is ensured, a simplified motion model can be used for motion estimation according to (13). This is shown in Fig. 9c for a fixed sensor S_1 at position $[x_1, y_1]=[3\,\mathrm{m}, 0\,\mathrm{m}]$. Here, almost independent of the position and orientation of the second sensor, a precise orientation estimate can be guaranteed with an accuracy smaller than $0.1°$.

Since a yaw rate of $\omega=0$ can't be ensured in reality, and the algorithm is to be applied in arbitrary scenarios, there is also the possibility to estimate the orientation of all sensors in the network with higher accuracy with the help of a third sensor, which is shown in Fig. 9d. Here, the two fixed sensors are located at positions $[x_1, y_1]=[3\,\mathrm{m}, 0\,\mathrm{m}]$ and $[x_2, y_2]=[0\,\mathrm{m}, 1\,\mathrm{m}]$. Especially compared to Fig. 9a and Fig. 9b, an almost position-independent estimation quality can be obtained even for curved trajectories. The average orientation estimation accuracy for this sensor constellation with $N=3$ sensors is approximately $0.25°$.

IX. CONCLUSION

Two sequential algorithms for an efficient orientation estimation of distributed radar sensors on a vehicle have been presented in this work. It was shown that for both straight-line and curved trajectories, the orientation of all radar sensors in the network can be estimated solely based on target lists. The optimal sensor positioning to achieve the best orientation estimates was presented and evaluated using a Monte-Carlo simulation for different networks. In addition, it was demonstrated by measurement studies to what extent the estimation improves with increasing number of sensors or increasing number of evaluated frames. It was shown that the orientation of the sensors can be determined with an accuracy of up to $0.26°$ exclusively based on arbitrary chosen targets for straight and curved trajectories. This is significantly more accurate than the standard deviation of the angle estimate of the radar sensor used. The independence towards all additional sensors like IMU or GNSS as well as the arbitrary positioning and orientation of the radar sensors without any restrictions or overlapping field of views allows the utilization in many application areas.

REFERENCES

[1] M. Mielle, M. Magnusson, and A. Lilienthal, "A comparative analysis of radar and lidar sensing for localization and mapping," in *European Conference on Mobile Robots (ECMR)*, 2019, pp. 1–6.

[2] T. Grebner, P. Schoeder, V. Janoudi, and C. Waldschmidt, "Radar-Based Mapping of the Environment: Occupancy Grid-Map Versus SAR," *IEEE Microwave and Wireless Components Letters*, vol. 32, no. 3, pp. 253–256, 2022.

[3] A. Frischen, J. Hasch, and C. Waldschmidt, "Contour recognition with a cooperative distributed radar sensor network," in *IEEE MTT-S Int. Conf. Microw. Intell. Mobil. (ICMIM)*, 2015, pp. 1–4.

[4] C. Waldschmidt, J. Hasch, and W. Menzel, "Automotive Radar — From First Efforts to Future Systems," *IEEE J. Microw.*, vol. 1, pp. 135–148, 2021.

[5] J. Pierre and M. Kaveh, "Experimental Performance of Calibration and Direction-Finding Algorithms," in *Int. Conf. on Acoust., Speech, and Signal Process.*, 1991, pp. 1365–1368 vol.2.

[6] C. Vasanelli, F. Roos, A. Durr, J. Schlichenmaier, P. Hugler, B. Meinecke, M. Steiner, and C. Waldschmidt, "Calibration and Direction-of-Arrival Estimation of Millimeter-Wave Radars: A Practical Introduction," *IEEE Antennas Propag. Mag.*, vol. 62, no. 6, pp. 34–45, 2020.

[7] A. Dürr, M. Linder, D. Schwarz, and C. Waldschmidt, "Highly Efficient Angular Array Calibration Based on the Modal Wave Expansion Technique," *IEEE Open J. Antennas Propag.*, vol. 2, pp. 938–948, 2021.

[8] L. Heng, "Automatic Targetless Extrinsic Calibration of Multiple 3D LiDARs and Radars," in *IEEE Int. Conf. Intell. Robots Syst. (IROS)*, 2020, pp. 10 669–10 675.

[9] B. Hui, G. Wen, P. Zhang, and D. Li, "A Novel Line Scan Camera Calibration Technique With an Auxiliary Frame Camera," *IEEE Trans. Instrum. Meas.*, vol. 62, no. 9, pp. 2567–2575, 2013.

[10] Y. Liu, Q. Wang, J. Liu, J. Chen, and T. Wark, "An Efficient and Effective Localization Method for Networked Disjoint Top-View Cameras," *Instrumentation and Measurement, IEEE Transactions on*, vol. 62, pp. 2526–2537, 09 2013.

[11] B. Fu, Y. Wang, X. Ding, Y. Jiao, L. Tang, and R. Xiong, "LiDAR-Camera Calibration Under Arbitrary Configurations: Observability and Methods," *IEEE Trans. Instrum. Meas.*, vol. 69, no. 6, pp. 3089–3102, 2020.

[12] L. Zhou and Z. Deng, "A New Algorithm for the Extrinsic Calibration of a 2D LIDAR and a Camera," *Meas. Sci. Technol.*, vol. 25, no. 6, p. 065107, 2014.

[13] D. Kellner, M. Barjenbruch, K. Dietmayer, J. Klappstein, and J. Dickmann, "Joint Radar Alignment and Odometry Calibration," in *18th Int. Conf. on Inf. Fusion (Fusion)*, 2015, pp. 366–374.

[14] Y. Bao, T. Mahler, A. Pieper, A. Schreiber, and M. Schulze, "Motion Based Online Calibration for 4D Imaging Radar in Autonomous Driving Applications," in *German Microwave Conference (GeMiC)*, 2020, pp. 108–111.

[15] R. Izquierdo, I. Parra, D. Fernández-Llorca, and M. A. Sotelo, "Multi-Radar Self-Calibration Method using High-Definition Digital Maps for Autonomous Driving," in *21st Int. Conf. on Intell. Transp. Syst. (ITSC)*, 2018, pp. 2197–2202.

[16] J. Oh, K.-S. Kim, M. Park, and S. Kim, "A Comparative Study on Camera-Radar Calibration Methods," in *Int. Conf. on Control, Atom., Robot. and Vision (ICARCV)*, 2018, pp. 1057–1062.

[17] C. Schöller, M. Schnettler, A. Krämmer, G. Hinz, M. Bakovic, M. Guzet, and A. Knoll, "Targetless Rotational Auto-Calibration of Radar and Camera for Intelligent Transportation Systems," in *IEEE trans. Intell. Transp. Syst.)*, 2019, pp. 3934–3941.

[18] C. Chou, S.-H. Yeh, and D. Song, "Mirror-assisted calibration of a multi-modal sensing array with a ground penetrating radar

and a camera," in *IEEE Int. Conf. Intell. Robots Syst. (IROS)*, 2017, pp. 1457–1463.

[19] K. T. Olutomilayo, M. Bahramgiri, S. Nooshabadi, and D. R. Fuhrmann, "Extrinsic Calibration of Radar Mount Position and Orientation With Multiple Target Configurations," *IEEE Trans. Instrum. Meas.*, vol. 70, pp. 1–13, 2021.

[20] M. Z. Ikram and A. Ahmad, "Automated Radar Mount-Angle Calibration in Automotive Applications," in *IEEE Radar Conf. (RadarConf)*, 2019, pp. 1–5.

[21] T. Grebner, M. Linder, N. Kern, P. Schoeder, and C. Waldschmidt, "6d self-calibration of the position and orientation of radar sensors in a radar network," in *19th European Radar Conf. (EuRAD)*, 2022, pp. 157–160.

[22] A. G. Stove, "Linear FMCW Radar Techniques," *IEE Proc. F Radar Signal Process.*, vol. 139, no. 5, pp. 343–350, 1992.

[23] H. Rohling and M.-M. Meinecke, "Waveform design principles for automotive radar systems," in *CIE Int. Conf. on Radar Proc. (Cat No.01TH8559)*. IEEE, 2001, pp. 1–4.

[24] V. Winkler, "Range Doppler Detection for Automotive FMCW Radars," in *Eur. Microw. Conf. (EuMC)*, Oct. 2007, pp. 1445–1448.

[25] D. Kellner, M. Barjenbruch, J. Klappstein, J. Dickmann, and K. Dietmayer, "Instantaneous Ego-Motion Estimation using Doppler Radar," in *16th IEEE trans. Intell. Transp. Syst. (ITSC)*, 2013, pp. 869–874.

[26] D. Kellner, M. Barjenbruch, J. Klappstein, J. Dickmann, and K. Dietmayer, "Instantaneous ego-motion estimation using multiple Doppler radars," in *IEEE Int. Conf. Robot. Autom. (ICRA)*, May 2014, pp. 1592–1597.

[27] T. Grebner, P. Schoeder, F. Konrad, and C. Waldschmidt, "Instantaneous Ego-Motion Estimation based on Ambiguous Velocity Information within a Network of Radar Sensors," in *14th German Microw. Conf. (GeMiC)*, 2022, pp. 140–143.

[28] M. A. Fischler and R. C. Bolles, "Random sample consensus: a paradigm for model fitting with applications to image analysis and automated cartography," *Commun. ACM*, vol. 24, pp. 381–395, 1981.

[29] D. Kong, W. Wen, R. Zhao, Z. Lv, K. Liu, Y. Liu, and Z. Gao, "Vehicle Lateral Velocity Estimation Based on Long Short-Term Memory Network," *World Electr. Veh. J.*, vol. 13, p. 1, 2021.

[30] M. Steiner, M. Keller, J. Geiß, M. Vossiek, and C. Waldschmidt, "Synchronization of Radar Sensors in a Network Based on Inter-Sensor Interference," in *16th European Radar Conference (EuRAD)*, 2019, pp. 229–232.

[31] H. Griffiths, "Radar System Analysis and Modeling." *The Aeronautical Journal*, vol. 109, p. 591, 2005.

Timo Grebner (Graduate Student Member, IEEE) received the master's degree in electrical engineering from Ulm University, Ulm, Germany, in 2019, where he is currently pursuing the Ph.D. degree in electrical engineering at the Institute of Microwave Engineering. In 2018, he was an Intern with Sony, Japan.

His current research interest includes the creation of high-resolution occupancy gridmaps by highaccuracy ego-motion estimations in a distributed and collaborative radar sensor topology.

Vinzenz Janoudi received the M.Sc. degree in electrical engineering from the University of Applied Sciences of Karlsruhe, Karlsruhe, Germany, and the M.Eng degree from Toronto Metropolitan University, Toronto, ON, Canada, in 2018 and 2019, respectively. He is currently working toward the Ph.D. degree in electrical engineering with the Institute of Microwave Engineering, University Ulm, Ulm, Germany.

In 2015 and 2016, he was with Rohde & Schwarz, Munich, as a Bachelor Thesis Student and Development Engineer for software defined radio waveforms. In 2018, he was with Bosch Corporate Research as a Master thesis Student in the field of distributed source coding. From 2019 to 2020, he was with PLATH Group as a Development Engineer for signal intelligence receivers and direction finders. Since 2020, he has been a Research Assistant with the University Ulm. His research interests include communication systems, stochastic signal processing, system concepts for radar networks in the automotive sector, and the accompanying signal processing.

Pirmin Schoeder (Graduate Student Member, IEEE) received the B.Sc. and M.Sc. degrees in 2017 and 2019, respectively, in electrical engineering from the University of Ulm, Ulm, Germany, where he is currently working toward the Ph.D. degree with the Institute of Microwave Engineering. In 2019, he was an Intern with Rohde & Schwarz, Singapore.

His current research interests include system concepts and signal processing for radar target simulators.

Christian Waldschmidt (Senior Member, IEEE) received the Dipl.-Ing. (M.S.E.E.) and the Dr.-Ing. (Ph.D.E.E.) degrees from the University Karlsruhe, Karlsruhe, Germany, in 2001 and 2004, respectively.

From 2001 to 2004, he was a Research Assistant with the Institut für Höchstfrequenztechnik and Elektronik, Universität Karlsruhe. Since 2004, he has been with Robert Bosch GmbH, in the business units Corporate Research and Chassis Systems. He was heading different research and development teams in microwave engineering, rf-sensing, and automotive radar. In 2013, he returned to academia. He was appointed as the Director of the Institute of Microwave Engineering, University Ulm, Ulm, Germany, as Full Professor. He has authored or coauthored more than 200 scientific publications and more than 20 patents. His research topics include on radar and rf-sensing, mm-wave and submillimeterwave engineering, antennas and antenna arrays, and rf and array signal processing. He is a Member of the Executive Committee Board of the German MTT/AP joint chapter, and Member of the German Information Technology Society. He is Chair of the IEEE MTT-29 Technical Committee on Microwave Aerospace Systems and was the Chair of MTT-27 Technical Committee on Wireless Enabled Automotive and Vehicular Applications. He was a two-time TPC Chair and General Chair of the IEEE MTT International Conference on Microwaves for Intelligent Mobility. Since 2018, he has been an Associate Editor for IEEE MTT MICROWAVE WIRELESS COMPONENTS LETTERS. He is a reviewer for multiple IEEE transactions and many IEEE conferences in the field of microwaves. He was co-recipient of 13 best paper awards since 2014.